Tailoring hydrogel mesh structure through custom-designed poly(ether urethane)s for advanced drug delivery systems in biomedical applications

Materials Advances

ROYAL SOCIETY OF CHEMISTRY

PAPER

Published on 11 August 2026

Cite this: DOI: 10.1039/d6ma00816j

Tailoring hydrogel mesh structure through custom-designed poly(ether urethane)s for advanced drug delivery systems in biomedical applications

Roberta Pappalardo, †[ab] Monica Boffito, †*[a] Claudio Cassino, [cd] Alessandra Flori, [e] Luca Menichetti, [e] Irene Carmagnola, [a] Valeria Chiono [a] and Gianluca Ciardelli [ab]

Hydrogel mesh size plays a pivotal role in determining physico-chemical and mechanical properties, making these materials versatile for tissue engineering and drug delivery applications. Herein, we report the tunability of mesh size in Schiff-base hydrogels through tailored poly(ether urethane) (PEU) chemistry. Three aldehyde-terminated PEUs (PEU-CHO) with different molecular weights ($\bar{M}_n$ = 1.6–9 kDa, $D \approx 1.4$) were synthesized and employed as crosslinkers for a high-molecular-weight amine-functionalized PEU (PEU-NH_2, $\bar{M}_n$ = 25 kDa, D = 1.7). Hydrogels formed upon mixing PEU aqueous solutions and underwent gelation within a few hours. Rheology revealed highly strain-resistant gels (up to 1200%) with tunable mechanical properties and mesh sizes of 18–50 nm. Thermal analyses showed ≈60% of freezable water and similar distributions in pore size (2 nm–2 μm). Notably, mesh size strongly affected the fluid uptake, the swelling behavior monitored in real-time *via* Magnetic Resonance Imaging, and the diffusion of model molecules. Smaller-mesh hydrogels exhibited diffusion-driven release for fluorescein isothiocyanate-dextran (FD) with $\bar{M}_w$ = 4 and 10 kDa, whereas anomalous diffusion occurred for FD 70 kDa, confirming network-hindered transport. This work provides a versatile strategy of molecular design to finely regulate hydrogel structure and performance, enabling the development of tailored biomaterials in the biomedical field.

Received 4th June 2026,
Accepted 10th August 2026

DOI: 10.1039/d6ma00816j

rsc.li/materials-advances

1. Introduction

Hydrogels have represented a significant advancement in biomedical applications, due to their high versatility, biocompatibility, and resemblance to soft tissues. These highly hydrated three-dimensional polymeric networks are able to absorb and retain significant amounts of water and biological fluids,[1] thereby closely mimicking the properties of the extracellular matrix of natural tissues. Their high water content, remarkable swelling ability, and soft consistency provide significant advantages, creating a favourable environment for interaction with the biological milieu to support processes such as cell adhesion, proliferation, and differentiation.[2] Furthermore, hydrogels can actively interact with the biological environment by undergoing changes in response to external stimuli (*e.g.*, pH, temperature, light), fulfilling specific physiological or therapeutic needs at the appropriate time and location.[3–5]

At the micrometer level, hydrogels result from the crosslinking of polymer chains *via* physical interactions (*e.g.*, ionic and hydrophobic interactions, hydrogen bonding) or chemical bonds (*e.g.*, Schiff-base, Diels–Alder, thiol–ene bonds).[6] A comprehensive knowledge of the composition and microstructure of the hydrogel is essential to better correlate its structural properties with macroscopic features.[7–9] Mathematical models can be applied to determine network parameters, such as mesh size, crosslinking density, and the average molecular weight between two adjacent crosslinking points, enabling the prediction of properties and the design of systems tailored to specific applications.[10–13] In this regard, numerous studies have investigated how the internal structure of the hydrogel impacts performance in tissue engineering and drug delivery; for

[a] *Department of Mechanical and Aerospace Engineering, Politecnico di Torino, 10129, Turin, Italy. E-mail: monica.boffito@polito.it*
[b] *Department of Life Sciences, Università di Modena e Reggio Emilia, 41125, Modena, Italy*
[c] *Department of Science and Technological Innovation, Università del Piemonte Orientale, 15121, Alessandria, Italy*
[d] *Magnetic Resonance Platform (PRISMA-UPO), Università del Piemonte Orientale, 15121, Alessandria, Italy*
[e] *Institute of Clinical Physiology, National Research Council (CNR), 56124, Pisa, Italy*
† Equal contribution.

instance, it has been demonstrated that increasing the crosslinking density modulates cell proliferation by increasing the number of adhesion sites,[14,15] while smaller mesh sizes enhance the capacity to load and retain drugs.[16]

The modulation of hydrogel structure can be achieved through different strategies, commonly related to the design of hydrogel formulations. For instance, Rehmann *et al.* reported the development of poly(ethylene glycol) (PEG)-based hydrogels with mesh sizes ranging between approximately 5 and 15 nm by varying the PEG concentration and molecular weight. The mesh size prediction allowed the description of protein release mechanism from the hydrogel.[17] Similarly, Tong *et al.* described a method to control the protein release from poly(ethylene glycol)-based hydrogels by changing the hydrogel concentration and the molecular weight of the polymer. Indeed, a reduction in mesh size was found to prevent burst release, enhance protein retention, and prolong release.[18] Bian *et al.* successfully tuned the crosslinking density of hydrogels based on photo-crosslinked hyaluronic acid by changing either the macromer concentration or the photopolymerization reaction time. Furthermore, the potential application of hyaluronic acid-based hydrogels as 3D models to promote chondrogenesis was related to the optimal crosslinking density, highlighting that increasing crosslinking density led to a reduction in the deposition of cartilage matrix by mesenchymal stem cells.[19]

Within this framework, poly(ether urethane)s (PEUs) have emerged as highly promising candidates for hydrogel formulation due to their inherent structural versatility and modularity, enabling a superior degree of physico-chemical tailoring.[20–22] Although PEU-based hydrogels have already been investigated for drug delivery applications,[23] a systematic study directly correlating the molecular design of the PEU precursors with the resulting network architecture has not been reported yet. To address this, the present study introduces a novel multi-scale approach that bridges the gap between polymer chemistry and macroscopic performance. Specifically, new hydrogels were developed through the Schiff-base crosslinking of customized PEUs. The modulation of the hydrogel mesh was achieved by using aldehyde-terminated PEUs of differing molecular weights as crosslinkers for a high molecular weight PEU bearing pendant primary amines. The formulations were thoroughly characterized using different methodologies, including rheological characterization, thermal analysis, stability tests, Magnetic Resonance Imaging (MRI), and diffusion tests of probe molecules. This approach, combining complementary experimental techniques and mathematical modelling, was employed to investigate the architecture of the hydrogel network and predict how polymer design affects mesh size and performance, providing key insights for the development of advanced drug delivery platforms.

2. Experimental

2.1. Materials

Poly(ethylene glycol) (PEG3350, $\bar{M}_n$ 3350 Da, PEG600 $\bar{M}_n$ 600 Da, PEG1500 $\bar{M}_n$ 1500 Da and PEG6000 $\bar{M}_n$ 6000 Da), 1,6 hexamethylene diisocyanate (HDI), dibutyltin dilaurate (DBTDL), and N-Boc serinol (N-Boc) were purchased from Sigma-Aldrich, Milan, Italy. 4-Hydroxybenzaldehyde (BA) was purchased from TCI Chemicals, Zwijndrecht, Belgium. As a solvent for PEU synthesis, tetrahydrofuran (THF) was purchased from Thermo Fisher, Kandel, Germany, while all other analytical grade solvents were purchased from Carlo Erba Reagents, Cornaredo, Italy. All the reagents and solvent for PEU synthesis were dried before use.[24]

2.2. Synthesis of a poly(ether urethane) bearing pendant primary amino groups

The PEU bearing pendant primary amines was synthesized as reported in our previous work.[24] Briefly, the synthesis was carried out in a one-step process by reacting PEG3350 (dried and melted according to our previously published protocol) and N-Boc (5% w/v in anhydrous THF) at a 1 : 1 molar ratio with HDI (at a 1 : 1 with respect to PEG3350 and N-Boc), in presence of DBTDL as a catalyst (0.1% w/w with respect to PEG3350 and N-Boc). The reaction was conducted for 10 min at 70 °C, and it was stopped by adding methanol to passivate any residual isocyanate groups. The synthesized PEU was collected by precipitation in petroleum ether (4 : 1 v/v with respect to THF), re-solubilized in THF at 30% w/v and purified in diethyl ether (5 : 1 v/v with respect to THF). Subsequently, to remove the Boc-protecting groups and expose the amino groups, the PEU (4% w/v) was subjected to an acidic treatment in the presence of chloroform and trifluoroacetic acid (80 : 20 v/v). The PEU exposing primary amino groups was referred to as SHE3350.

2.3. Synthesis of aldehyde-terminated poly(ether urethane)s with different molecular weight

Aldehyde-terminated PEUs (coded as AHE600, AHE1500 and AHE6000) were synthesized through a two-step synthesis procedure, by selecting poly(ethylene glycol) with an appropriate molecular weight (PEG600, PEG1500, and PEG6000), HDI and BA as building blocks. Specifically, the PEU AHE1500 was synthesized according to the optimized method reported in our previous work.[24] Briefly, PEG1500 (dried and melted according to our previously published protocol) was solubilized in anhydrous THF at 30% w/v and added with HDI and DBTDL (at a 2.1 : 1 molar ratio and 0.1% w/w with respect to PEG1500, respectively). After 30 min at 60 °C, BA was added (13% w/v in THF, 2.1 : 1 molar ratio with respect to PEG1500), and the reaction was conducted for 2.5 h at 60 °C. Similarly, the PEUs AHE600 and AHE6000 were synthesized by end-capping isocyanate-terminated prepolymers. These prepolymers resulted from the pre-polymerization of PEG600 or PEG6000 (30% w/v in anhydrous THF) with HDI in the presence of DBTDL as a catalyst (at a 2.1 : 1 molar ratio and 0.1% w/w with respect to PEG600 or PEG6000, respectively). The first step was carried out for 15 min at 60 °C. Then, BA was added at 13% w/v in anhydrous THF at a 2.1 : 1 molar ratio with respect to PEG6000 or PEG600. The second step was conducted for 2.5 h at 60 °C, and the reaction was stopped by addition of methanol (MeOH, 6 mL per 16 g of theoretically synthesized PEU). The aldehyde-terminated PEUs were collected by precipitation in

petroleum ether (at a 4 : 1 v/v ratio with respect to THF). Then, PEUs were purified by solubilization in THF at 30% w/v and a further precipitation in diethyl ether (at a 5 : 1 v/v ratio with respect to THF).

Finally, the collected PEUs were dried under a fume hood and stored under an inert atmosphere at 4 °C until use.

2.4. Chemical characterization of poly(ether urethane)s

To prove the success of their synthesis, all the *ad hoc* synthesized poly(ether urethane)s (PEUs) (*i.e.*, SHE3350, AHE600, AHE1500, AHE6000) were chemically characterized through Attenuated Total Reflectance-Fourier Transform Infrared (ATR-FTIR) spectroscopy, Size Exclusion Chromatography (SEC), and Proton Nuclear Magnetic Resonance (^{1}H NMR) spectroscopy, according to the methods reported in our previous work.[24] A detailed description of the experimental protocols is reported in the SI.

2.5. Preparation and characterization of hydrogels based on Schiff-base crosslinking

2.5.1. Hydrogels preparation and tube inverting test. Three hydrogels based on Schiff-base crosslinking were formulated by blending SHE3350 with either AHE1500 (SHE3350–AHE1500) or AHE6000 (SHE3350–AHE6000) or a mixture of AHE6000 and AHE600 (SHE3350–AHE6000 + AHE600). The hydrogels were prepared at an overall polymer concentration of 20% w/v with a $-NH_2$: –CHO 3 : 1 molar ratio, in accordance with the hydrogel composition that was optimized in our previous work.[24] The formulation comprising only AHE600 as the aldehyde-terminated PEU was not developed due to the low solubility of this polymer in water (water solubility limit 0.35% w/v) that did not allow to achieve the concentration and the $-NH_2$: –CHO molar ratio requested for the formulation of the hydrogel. As for SHE3350–AHE1500 and SHE3350–AHE6000, each PEU was first solubilized in a volume of double-distilled water (*i.e.*, ddH_2O) equal to half of the total required volume for hydrogel preparation and the hydrogels were simply prepared by mixing the PEU solutions for 30 s using a system of double poly(propylene) (PP) syringes (LLG International, Germany) with a luer-lock connection. Conversely, in case of SHE3350–AHE6000 + AHE600 formulation, AHE6000 was solubilized in an aqueous solution of AHE600 (previously prepared at 0.32% w/v concentration) and in a volume corresponding to half of the total volume of the gel. Then, the AHE6000 + AHE600 solution was mixed with the SHE3350 aqueous solution to get the SHE3350–AHE6000 + AHE600 hydrogel formulation according to the protocol described for SHE3350–AHE1500 and SHE3350–AHE6000. Lastly, the resulting polymer solutions were transferred into a Bijou sample container (17 mm diameter, 7 mL, Carlo Erba Reagents, Cornaredo, Italy) and vortexed at 1500 rpm for 60 seconds.

The gelation time of the three formulations was tested in physiological-like conditions through the tube inverting test. Briefly, samples were incubated at 37 °C (Memmert IF75, Schwabach, Germany) and visually inspected after vial inversion at different time steps (*i.e.*, 15, 30, 45, 60 min, 2, 3, 4, 5, 6, 7, 8, 9, 10, 12, 24 h). The time of the sol-to-gel transition was evaluated based on the absence of flow along the vial walls within 30 s of inversion.

2.5.2. Rheological characterization and structural properties of hydrogels. The rheological characterization was performed using a stress-controlled rheometer (MCR302, Anton Paar GmbH, Graz, Austria) equipped with a Peltier system for the control of temperature and a configuration of 15 mm parallel plates. Samples were loaded in the gel state on the lower plate, which was equilibrated at 25 °C. Strain sweep tests were conducted from 0.01 to 1200% strain, at 37 °C, 1 Hz and 0 N normal force. Frequency sweep tests were performed at 37 °C, 0.5% strain (within the linear viscoelastic region defined through the strain sweep test) and 0 N normal force, within an angular frequency range between 0.1 and 100 rad s^{-1}.

The rheological characterization was also used to evaluate the structural parameters of the hydrogels (crosslinking density ρ, mol m^{-3}, and mesh size ξ, nm), according to eqn (1) and (2), respectively:

$$\rho = \frac{G'}{R \times T} \quad (1)$$

$$\xi = (\rho \times N_A)^{-1/3} \quad (2)$$

where G' (Pa) is the value of the elastic modulus at the plateau region measured through the frequency sweep test at 37 °C, R is the universal gas constant (8.314 J K^{-1} mol^{-1}), T is the temperature (K) and N_A is the Avogadro constant.[25–27] Analyses were performed in triplicate and results are reported as the mean ± standard deviation.

2.5.3. Thermal analysis and hydrogel water content. Differential scanning calorimetry (DSC) was performed on the Schiff-base hydrogels using a NEXTA© DSC200 instrument (Hitachi, Japan). SHE3350–AHE1500, SHE3350–AHE6000 and SHE3350–AHE6000 + AHE600 were prepared according to the protocol reported above. Each sample (10–15 mg) was transferred immediately after the mixing of polymer solutions into a hermetic pan and sealed. To ensure complete gelation, the hydrogels were analyzed 24 hours after sample preparation. Samples were cooled from 20 °C to −40 °C at 2 °C min^{-1}, isothermally controlled at −40 °C for 10 min and finally heated from −40 °C to 70 °C at 2 °C min^{-1}, under a flow of argon. Analyses were performed in triplicate, and results are reported as the mean ± standard deviation.

The states of water within the hydrogels after crosslinking (EWC equilibrium water content, W_f freezable water content, and W_{nf} non-freezable water content) were determined using eqn (3)–(5):

$$\mathrm{EWC}\ (\%) = \frac{w_{wet} - w_{dry}}{w_{wet}} \times 100 \quad (3)$$

$$W_f\ (\%) = \frac{Q_m}{\Delta H_m} \times 100 \quad (4)$$

$$W_{nf}\ (\%) = \mathrm{EWC} - W_f \quad (5)$$

where w_{wet} and w_{dry} are the wet weight and the dry weight of the sample after crosslinking, respectively. Q_m (J g^{-1}) is the sum of the enthalpy changes obtained by linearly integrating the endothermic melting peaks recorded by the DSC analysis and calculated through the NEXTA© TA software, while ΔH_m is the enthalpy of bulk water (333.5 J g^{-1}).[28]

The pores size and their dimensional distribution within the gel network were calculated from the melting point of water molecules confined into small pores. Briefly, considering spherical pores filled with water as condenser, the pore radius R_p (nm) and the distribution of the pore volume dV/dR_p (cm^3 g^{-1} nm^{-1}) were determined from eqn (6) and (7):

$$R_p = -\frac{32.33}{\Delta T} + 0.68 \quad (6)$$

$$\frac{dV}{dR_p} = \frac{\Delta V}{R_i - R_{i+1}} \quad (7)$$

where $\Delta T = T - T_0$ is the triple point depression of water, with T_0 being the triple point of water (273.16 K), ΔV is the pore volume and $R_i - R_{i+1}$ values are the pore radii corresponding to consecutive points of temperature.[29,30] A detailed description of the calculations is provided in the SI.

2.5.4. Hydrogel stability in aqueous environments. The hydrogel behavior in aqueous environments was tested by sample incubation in contact with aqueous media at 37 °C (Memmert IF75, Schwabach, Germany). In detail, 0.5 mL of each formulation was prepared according to the method reported above. The initial sample weight was recorded, and the hydrogels were equilibrated at 37 °C for 30 min. Afterwards, 1 mL of phosphate-buffered saline (PBS at pH 7.4, Sigma Aldrich-Merck, Milan, Italy) or phosphate buffer at pH 5 was added to each sample. At selected time points (*i.e.*, 7, 24 h, 3, 6, 8, 10, 13, 15, 17, 20, 22, 24, and 27 days), the residual buffer solution was removed, the samples were weighed to register their wet weight and then put again in contact with 1 mL of fresh buffer. After 27 days of incubation, the samples were freeze-dried and weighed. As reference, SHE3350–AHE1500, SHE3350–AHE6000 and SHE3350–AHE6000 + AHE600 samples that were not incubated in contact with aqueous media were also lyophilized and weighed. Lastly, the fluid absorption (percentage of change in wet weight) and hydrogel dissolution after 27 days of incubation (percentage of change in dry weight) were calculated according to the equations already published.[24] The tests were performed in triplicate and results are reported as the mean ± standard deviation.

2.5.5. Hydrogel fluid absorption monitoring through Magnetic Resonance Imaging (MRI). The hydrogel behaviour in contact with an aqueous environment was also studied by applying the Magnetic Resonance Imaging (MRI) technique. The MRI analyses were performed using a vertical wide bore Bruker III HD 300 MHz spectrometer (7 T). The instrument was equipped for micro-imaging. The analyses were conducted at 37 °C, using a ^{1}H volume coil (with a diameter of 30 mm). T_1- and T_2-weighted images were obtained by selecting the sequences and parameters reported in Table 1.

The recorded T_1-weighted and T_2-weighted images were analyzed using the Paravision 6.0.1-Image Sequence Analysis (ISA) Tool software (Bruker).

The hydrogels were prepared according to the procedure described above. Briefly, 1.5 mL of SHE3350–AHE1500, SHE3350–AHE6000 and SHE3350–AHE6000 + AHE600 hydrogels were prepared by simply mixing the polymer solutions; the mixtures were then transferred into an NMR tube with a diameter of 10 mm. After complete gelation (achieved through incubation at room temperature for 24 h), hydrogel behaviour in physiological-like conditions was tested by incubating the samples in contact with 3 mL of a phosphate-buffered saline (PBS, pH 7.4) solution at 37 °C. At predefined time steps (*i.e.*, 4 and 24 hours, 3, 6, and 10 days), the residual buffer was removed, the MR images of the samples were acquired, and 3 mL of fresh PBS were added. Changes in the thickness of the hydrogel were measured according to eqn (8):

$$\text{Dimension change } (\%) = \frac{h_x - h_i}{h_i} \times 100 \quad (8)$$

where h_i and h_x are the thickness values of the hydrogel measured from the T_1-weighted and T_2-weighted images before incubation and at each predefined time point, respectively.

2.6. Release and diffusivity study of probe molecules

2.6.1. Release of fluorescein isothiocyanate-dextran molecules. The release profile and mechanism of model molecules from the developed Schiff-base hydrogels were investigated in physiological-like conditions. Specifically, the release kinetics of fluorescein isothiocyanate-dextran (FD) molecules with $\bar{M}_w$ 4 kDa (FD4), 10 kDa (FD10) and 70 kDa (FD70) (Sigma Aldrich-Merck, Milan, Italy) were studied at pH 7.4 and 37 °C by loading the model molecules into the three formulations and incubating the samples in contact with PBS at 37 °C. In detail, SHE3350–AHE1500, SHE3350–AHE6000 and SHE3350–AHE6000 + AHE600 gels (0.5 mL) were prepared according to the previously reported protocol, using an aqueous solution containing FD (at 2 mg mL^{-1}) as the solvent. Upon gelation, the samples were equilibrated at 37 °C for 30 min and put in contact with 1 mL of phosphate-buffered saline at pH 7.4. At predefined time points (*i.e.*, 3.5, 7 and 24 h, 3, 6, 8, 10, 13, 15,

Table 1 Sequences and parameters to acquire T_1- and T_2-weighted images

	Sequence	TE (ms)	TR (ms)	Average	Flip-angle	Matrix size	FOV (mm^2)	Slice thickness (mm)
T_1	MSME	20	500	3	90°	128 × 128	24 × 35	1
T_2	MSME	50	2500	1	90°	128 × 128	24 × 35	1

MSME = Multi Slice Multi echo sequence, TE = Time to Echo, TR = Repetition Time, FOV = Field of View.

and 17 days), the release medium was collected, and the samples were added with 1 mL of fresh PBS. The amount of FD4, FD10 or FD70 released over time was quantified by measuring the absorbance at 490 nm through a plate reader (Perkin Elmer Victor X3) and by referring to calibration curves based on FD4, FD10 and FD70 standards with defined concentrations (ranging between 0.025 mg mL^{-1} and 1 mg mL^{-1} in PBS).

The mechanism of molecule release from the three formulations was studied by applying the Korsmeyer–Peppas model; the release rate constant k and release exponent n were calculated according to eqn (9):

$$\frac{M_t}{M_\infty} = k \times t^n \tag{9}$$

where M_t is the amount of released drug at a predefined time step t, and M_∞ is the amount of encapsulated FD.[31] Tests were conducted in triplicate and results are reported as mean ± standard deviation.

2.6.2. Diffusivity of fluorescein isothiocyanate-dextran molecules. The diffusion of solutes (FD4, FD10 and FD70) through the engineered Schiff-base hydrogels was also modeled and correlated with their structural properties. More in detail, starting from the hydrodynamic radius R of FD4, FD10 and FD70 (available from the supplier's datasheet), a theoretical estimation of their diffusion coefficients (D_0, $\mu m^2\ s^{-1}$) in water was obtained by applying the Stokes–Einstein eqn (10):

$$D_0 = \frac{kT}{6\pi\eta R} \tag{10}$$

where k is the Boltzmann constant (1.38×10^{-23} J K^{-1}), T is the absolute temperature (310.15 K), η is the viscosity of water at 37 °C (0.6915 mPa s) and R is the hydrodynamic radius of FD4, FD10 and FD70 (1.4 nm, 2.3 nm and 6 nm, from Sigma Aldrich-Merck datasheets, respectively).

Due to the presence of a polymeric network, the expected diffusion coefficients through the hydrogels (D_p^*, $\mu m^2\ s^{-1}$) could be estimated through the Lustig-Peppas model, which describes the relationship between solute diffusivity and network structure. D_p^* was calculated according to eqn (11):

$$\frac{D_p^*}{D_0} = \left(1 - \frac{R}{\xi}\right) \exp\left(-Y\left(\frac{v_{2c}}{1 - v_{2c}}\right)\right) \tag{11}$$

where ξ is the mesh size of the hydrogel derived from the rheological characterization, exp is the exponential function, Y can be approximated to 1, ν_{2c} is the fraction of the gel polymer, estimated as $\nu_{2c} = V_p/V_{gc}$, with V_p representing the volume of the dry polymer calculated from the freeze-dried gel mass and the polymer density (density of PEG in the dry state is 1.12 g cm^{-3}), and V_{gc} being the gel volume.[32]

Furthermore, the release results were fitted to the Fickian diffusion model to experimentally determine the diffusivity of fluorescein isothiocyanate-dextran through the hydrogel. Considering perfect sink conditions in the release medium during the experiment, and that the release mechanism is prevalently driven by diffusion, the diffusivity coefficients D_p can be estimated according to the analytical solution of the Fick's second law of diffusion, reported in eqn (12):

$$\frac{M_t}{M_\infty} = \left(\frac{16 D_p t}{\pi H^2}\right)^{0.5} \tag{12}$$

where M_t and M_∞ are the cumulative amount of released molecules from the hydrogel after a predefined time t and *ad infinitum*, respectively, and H is the thickness of the cylindrical hydrogel. D_p can be obtained from the slope of the linear portion of M_t/M_∞ *vs.* $t^{0.5}$, for $0 < M_t/M_\infty < 0.6$.[33]

2.7. Scanning Electron Microscopy (SEM)

A morphological characterization of the developed hydrogels was performed using Scanning Electron Microscopy (SEM). SHE3350–AHE1500, SHE3350–AHE6000 and SHE3350–AHE6000 + AHE600 hydrogels (1 mL) were prepared into a Bijou sample container (1.7 cm internal diameter), according to the previously reported method. Then, the samples were frozen at −20 °C and freeze-dried (Martin Christ ALPHA 2–4 LSC Instrument, Germany). Using a scanning electron microscope (Tescan Vega Magna, Brno, Czech Republic), SEM images were acquired from the cross-sections of the freeze-dried hydrogels, which were obtained by fracture in liquid nitrogen. Briefly, the samples were disposed on aluminium stubs using a carbon tape and coated with a platinum layer of 9 nm (High Resolution Sputter Coater, Agar Scientific, Stansted, United Kingdom), using a metallization current and pressure of 30 mA and 0.01 Pa, respectively, and Cr/Pt as target. Analyses were performed at different magnifications (30× and 100×).

2.8. Statistical analysis

Statistical analysis was performed using GraphPad Prism 10 for Windows 10 (GraphPad Software, La Jolla, CA, USA; https://www.graphpad.com). A Two-Way ANOVA analysis coupled with the Bonferroni's multiple comparison test was conducted to compare the results. Statistical differences were assessed according to Boffito *et al.*[20]

3. Results and discussion

3.1. Characterization of customized poly(ether urethane)s

A comprehensive physico-chemical characterization of the customized poly(ether urethane)s (PEUs) exposing pendant primary amino groups or aldehyde-end groups is reported in the SI. Briefly, ATR-FTIR spectroscopy was first conducted to confirm the success of the synthesis of poly(ethylene glycol)-based PEUs. Indeed the ATR-FTIR spectra of SHE3350, AHE600, AHE1500 and AHE6000 showed both new absorption bands ascribed to the formation of urethane bonds (at 3347 and 1720 cm^{-1} stretching vibrations of N–H and C═O, respectively, and at 1530 cm^{-1} concurrent N–H bending and C–N stretching vibrations) and the characteristic peaks of poly(ethylene glycol) (at 2876 cm^{-1} and 1110 cm^{-1} stretching vibration of $-CH_2$ and C–O–C, respectively) (Fig. S1).[24] Size Exclusion Chromatography (SEC) proved the successful synthesis of a high molecular

weight PEU (SHE3350, number-average molecular weight $\bar{M}_n$ 25 kDa and polydispersity index D 1.7), and three different low molecular weight PEUs (AHE600, $\bar{M}_n$ 1.6 kDa and D 1.4, AHE1500 $\bar{M}_n$ 4 kDa and D 1.5, AHE6000, $\bar{M}_n$ 9 kDa and D 1.2). ^{1}H NMR spectroscopy also confirmed the chemical nature of the new polymers, as all the spectra showed signals ascribed to the chemical structure of PEUs (Fig. S2).[24] Furthermore, concerning the PEU bearing pendant primary amines, the successful deprotection treatment and cleavage of N-Boc (100% deprotection yield) were demonstrated by comparing the ^{1}H NMR spectra of the Boc-protected SHE3350 and SHE3350. Finally, by referring to the spectrum of N-Boc serinol, the number of Boc groups and thus $-NH_2$ units resulted to be around 2×10^{20} per gram of SHE3350 (Fig. S3). Similarly, by referring to the spectrum of 4-hydroxybenzaldehyde (BA), the total amount of BA units was quantified to be *ca.* 1.2×10^{21} per gram of AHE600, 4×10^{20} per gram of AHE1500, and 9.9×10^{19} per gram of AHE6000 (Fig. S4).

3.2. Schiff-base crosslinked hydrogels with tunable structural properties

A plethora of chemically crosslinked hydrogels was formulated by mixing aqueous solutions of SHE3350 PEU, which exposed pendant primary amines, with aldehyde-terminated PEU AHE1500 or AHE6000, or a combination of AHE6000 and AHE600, being the latter poorly soluble in water to be used as a crosslinker alone. Hydrogels resulting from the spontaneous formation of Schiff-base bonds between the functionalities exposed by the PEU chains were first characterized in terms of physical, thermal and rheological properties. A schematic illustration of the PEU precursors and the mechanism of Schiff-base hydrogel formation by mixing the PEU aqueous solutions is reported in Fig. S5.

3.2.1. Hydrogel gelation time. The ability of the hydrogels to undergo sol-to-gel transition when polymers containing primary amines and aldehydes were mixed was first assessed through the tube inverting test performed at 37 °C. All the three Schiff-base hydrogels, prepared at an overall polymer concentration of 20% w/v and $-NH_2$: –CHO molar ratio of 3 : 1, underwent gelation within few hours, with some differences due to their different composition, as summarized in Table 2.

As previously reported, the time of the sol-to-gel transition of SHE3350–AHE1500 hydrogel was estimated to be 45 minutes,[24] while SHE3350–AHE6000 and SHE3350–AHE6000 + AHE600 underwent gelation within *ca.* 7 hours and 5 hours, respectively. This significantly different behaviour exhibited by the samples containing AHE6000 can be attributed to the lower total amount of –CHO groups per gram of AHE6000 (*i.e.*, 9.9×10^{19} *vs.* 4×10^{20} for AHE1500) and its higher molecular weight compared to AHE1500 (9 kDa *vs.* 4 kDa). These two concurrent factors directly affected the masses of the two components (PEU-NH_2 and PEU-CHO) weighted for the preparation of formulation at a fixed polymeric concentration (20% w/v) and molar ratio between the functionalities ($-NH_2$: –CHO 3 : 1 molar ratio). Indeed, due to the reduced quantity of chains of high molecular weight SHE3350 within the SHE3350–AHE6000 mixture (SHE3350 was *ca.* 60% by weight in SHE3350–AHE6000 *vs.* around 80% in SHE3350–AHE1500), the intimate interaction between the functionalities was most likely constrained, or, at least, delayed. Furthermore, due to its higher molecular weight, the mobility of the AHE6000 chains could be hypothesized to be lower in comparison to AHE1500. Finally, the overall viscosity of the formulation exerts a significant influence on the status of flow (or no-flow) of the system upon vial inversion. As the content of SHE3350 was reduced, the starting viscosity of SHE3350–AHE6000 decreased. Consequently, the achievement of the no-flow condition was delayed until a higher number of Schiff-base bonds formed, resulting in an increase in viscosity. Lastly, the additional presence of AHE600 in the SHE3350–AHE6000 + AHE600 formulation resulted in a slightly reduced gelation time compared to SHE3350–AHE6000. Indeed, the lower molecular weight of AHE600 in comparison to AHE6000 improved the mobility of the polymer chains, resulting in enhanced kinetics of aldehyde crosslinking with the pendant primary amines of the SHE3350 chains.

3.2.2. Rheological properties and definition of hydrogel structural parameters. The viscoelastic properties of the hydrogels crosslinked *via* Schiff-base were analyzed through rheological characterization. The results of strain sweep test (Fig. 1) showed the hydrogel response to the applied deformation. All the formulations were characterized by a broad region of linear viscoelasticity (*i.e.*, LVE limits of 120% for SHE3350–AHE1500 and 500% for both SHE3350–AHE6000 and SHE3350–AHE6000 + AHE600), demonstrating high resistance to the applied deformation. Within the LVE region, samples displayed constant elastic G' and viscous G'' moduli, with $G' > G''$, indicating that all the samples were in the gel state at the testing temperature of 37 °C. Concerning the mechanical

Table 2 Gelation time of SHE3350–AHE1500, SHE3350–AHE6000 and SHE3350–AHE6000 + AHE600 hydrogels, as defined through the tube inverting test at 37 °C

Sample	Gelation time
SHE3350–AHE1500	45 min
SHE3350–AHE6000	7 h
SHE3350–AHE6000 + AHE600	5 h

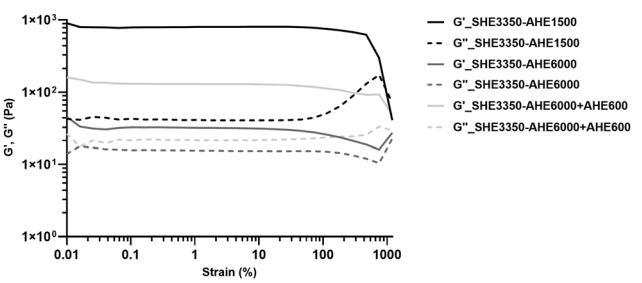

Fig. 1 Strain sweep test at 37 °C. Elastic modulus G' (continuous line) and viscous modulus G'' (dashed line) *vs.* applied deformation (from 0.01 to 1200% strain) for SHE3350–AHE1500 (black line), SHE3350–AHE6000 (grey line) and SHE3350–AHE6000 + AHE600 (light grey line).

properties, SHE3350–AHE6000 and SHE3350–AHE6000 + AHE600 exhibited lower G' values compared to SHE3350–AHE1500. Indeed, the latter exhibited a G' value at a strain of 1% of 800 Pa, compared to 32 Pa and 130 Pa for SHE3350–AHE6000 and SHE3350–AHE6000 + AHE600, respectively. Moreover, their highly soft nature allowed them to better accommodate the applied deformations, resulting in the impossibility of achieving a complete network breakage even at the highest value of deformation (*i.e.*, 1200% strain). Conversely, for SHE3350–AHE1500, G' and G'' started to increase and decrease, respectively, at around an applied strain of 200–300%, thus suggesting the formation of cracks within the network. Afterward, the gel rupture was observed at *ca.* 800–1000% of applied strain, with G'' becoming greater than G' ($G'' > G'$).

Frequency sweep tests were also performed on the three formulations at 37 °C. Fig. 2 shows the trends of the elastic G' and viscous G'' moduli as a function of angular frequency. All the tested formulations showed $G' > G''$, confirming their gel state at the testing temperature. SHE3350–AHE1500 exhibited a constant trend for G' over the range of analyzed angular frequency. Furthermore, for this sample, the difference between G' and G'' was higher than one order of magnitude, indicating that the formulation was a fully developed gel. Conversely, SHE3350–AHE6000 and SHE3350–AHE6000 + AHE600 showed a slight dependence of the elastic modulus G' on the angular frequency, indicating for these samples the achievement of less developed networks. However, the superior G'–G'' delta for SHE3350–AHE6000 + AHE600 indicated a higher degree of network development compared to SHE3350–AHE6000.

Considering that the arrangement of polymer chain exerts a pivotal role in determining the viscoelastic properties of the hydrogel, rheological analyses were also exploited to provide a structural characterization of hydrogel network in terms of average crosslinking density ρ and mesh size ξ, as summarized in Table 3.

According to the rubber elasticity theory, which establishes a correlation between network structure and elastic properties,[34] the crosslinking density was calculated to be 0.29 ± 0.07 mol m^{-3} for SHE3350–AHE1500, 0.013 ± 0.004 mol m^{-3} for SHE3350–AHE6000 and 0.051 ± 0.009 mol m^{-3} for SHE3350–AHE6000 + AHE600 ($p < 0.01$). As the crosslinking density is a function of the elastic modulus G', these results were in agreement with the reported outcomes regarding the mechanical properties. Indeed, the superior mechanical properties recorded for SHE3350–AHE1500 were related to its higher crosslinking density. Furthermore, as the mesh size is inversely related to the crosslinking density, the lower crosslinking density calculated for SHE3350–AHE6000 resulted in a larger mesh size, which was estimated to be *ca.* 50 nm compared to 32 nm for SHE3350–AHE6000 + AHE600 and 18 nm for SHE3350–AHE1500 ($p < 0.01$). Lastly, by directly comparing the three hydrogels that differed for the molecular weight of the aldehyde-terminated PEU, the trend of the mesh size was SHE3350–AHE6000 > SHE3350–AHE6000 + AHE600 > SHE3350–AHE1500, in agreement with the rheological outcomes described above. Hence, the determination of the structural parameters of the hydrogels from the mechanical characterization provided evidence of the tunability of the mesh size by properly selecting the materials that form the gel.

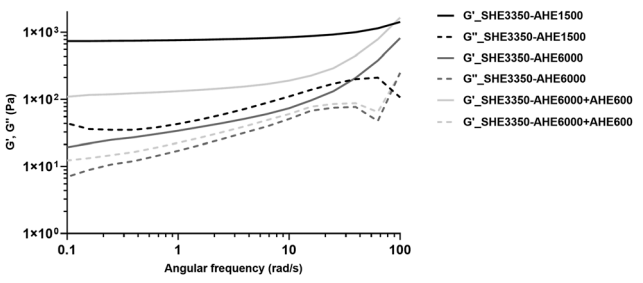

Fig. 2 Frequency sweep test at 37 °C. Elastic modulus G' (continuous line) and viscous modulus G'' (dashed line) *vs.* angular frequency (from 0.1 to 100 rad s^{-1}) for SHE3350–AHE1500 (black line), SHE3350–AHE6000 (grey line) and SHE3350–AHE6000 + AHE600 (light grey line).

Table 3 Structural parameters (*i.e.*, crosslinking density ρ and mesh size ξ) of SHE3350–AHE1500, SHE3350–AHE6000 and SHE3350–AHE6000 + AHE600 hydrogels. Parameters were estimated starting from rheological data (*i.e.*, G' at 1 rad s^{-1} from frequency sweep test at 37 °C)

Sample	G' (Pa)	ρ (mol m^{-3})	ξ (nm)
SHE3350–AHE1500	758.0 ± 197.0	0.29 ± 0.07	17.9 ± 1.5
SHE3350–AHE6000	33.9 ± 10.1	0.013 ± 0.004	50.7 ± 4.6
SHE3350–AHE6000 + AHE600	131.6 ± 24.1	0.051 ± 0.009	32.0 ± 2.0

3.2.3. States of water within hydrogels based on Schiff-base crosslinking and hydrogel porosity. Within the hydrogel network, water is the predominant constituent and is found in three primary states: (i) free or bulk water, which diffuses around the polymer chains; (ii) weakly bound water, resulting from weak interactions with the matrix; and (iii) tightly bound water, strongly associated with the hydrophilic portions of the polymer chains.[28] These states play a crucial role in determining the characteristics and performance of the hydrogel. To characterize the water content, a thermal analysis was conducted on the three developed Schiff-base crosslinked hydrogels. Specifically, DSC was employed to investigate the water states within the polymeric matrices of SHE3350–AHE1500, SHE3350–AHE6000 and SHE3350–AHE6000 + AHE600. The interaction between water molecules and the polymer chains at different molecular levels leads to the identification of distinct water states, which are characterized by diversified mobilities and, accordingly, abilities to crystallize. Based on this crystallization ability, water within hydrogels can be discerned in two fractions: (i) non-freezable bound water W_{nf}, which corresponds to the tightly bound water interacting with the polymer chains *via* hydrogen bonding; and (ii) freezable water W_f, which includes the free bulk water and the intermediate weakly bound water, minimally interacting with the polymeric counterpart of the hydrogel.[28,35] Average DSC thermograms of the recorded heating cycle for the three formulations are reported in Fig. 3. Melting temperatures and corresponding enthalpies are reported in the SI (Table S1). All the three thermograms showed two endothermic peaks, with

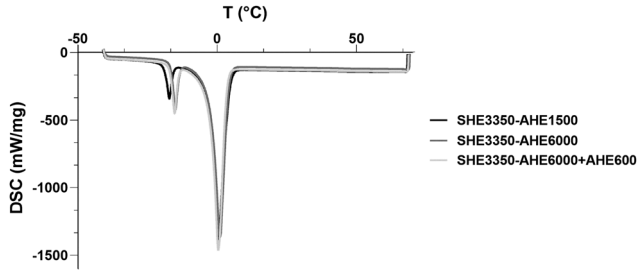

Fig. 3 DSC thermograms recorded for the developed Schiff-base hydrogels. Heating cycles (from −40 to 70 °C, 2 °C min^{-1}) for SHE3350–AHE1500 (black line), SHE3350–AHE6000 (grey line) and SHE3350–AHE6000 + AHE600 (light grey line).

melting temperatures centred at around 0 °C and between −20 and −15 °C. According to the literature, the latter could be associated with the melting of the intermediate freezable water confined within the small pores of the hydrogel, while the endothermic peak at around 0 °C could be referred to the freezable water inside the large pores and free water.[7,36]

The water content within the Schiff-base hydrogels after crosslinking was calculated by combining DSC and gravimetric data (Fig. 4). Since all the hydrogels were formulated at a polymer concentration of 20% w/v, the equilibrium water content (EWC) of SHE3350–AHE1500, SHE3350–AHE6000 and SHE3350–AHE6000 + AHE600 after preparation resulted to be approximately 83.6%, with no significant differences. The sum of the enthalpy changes of the endothermic melting peaks calculated from the DSC data allowed the calculation of the content of freezable water (W_f), according to eqn (4). The amount of W_f and the fraction of non-freezable water (W_{nf}) were quantified around 59.7% and 23.8%, respectively, with no significant differences among the three formulations. Irrespective of the gel composition, although the formulations showed different crosslinking density and mesh size, they resulted in a similar water content distribution within the hydrogel network. This trend could be elucidated by considering the interaction phenomena occurring between water molecules and polymer chains at the molecular level. Indeed, the total polar sites present on the poly(ethylene glycol)-based poly(ether urethane)s, which are responsible for the hydrogen bonding between water molecules and polymer chains, were found to be comparable for all hydrogels.

Furthermore, since the pore size of a porous material determines a decrease in the triple point temperature of a solvent that fills the pores compared to its bulk triple point,[37] the thermodynamic behaviour of the freezable bound water confined within the pores enabled the calculation of the pore radii distribution at the nano-scale level. All the three formulations were characterized by the presence of pores with radii ranging between 2 nm and 2 μm. However, the analysis of the pore size distribution revealed an intensification of the peaks at lower radii (2–20 nm), with a slight shift towards smaller sizes for SHE3350–AHE1500 compared to SHE3350–AHE6000 and SHE3350–AHE6000 + AHE600 (Fig. 5). Overall, since no significant differences were observed in terms of water states among the three formulations, the trends of pore size distribution confirmed the similarity of the formulations at the molecular level.

3.2.4. Schiff-base crosslinked hydrogels behaviour in physiological-like conditions. The evaluation of hydrogel behavior in contact with an aqueous environment in physiological-like conditions provided insight into the stability of the formulations, in terms of fluid absorption and dissolution over time. The designed Schiff-base crosslinked hydrogels were incubated in contact with phosphate buffer at pH 7.4, at 37 °C for up to 27 days. All the formulations were characterized by a high ability to absorb fluids and stability over time. After 24 hours of incubation, the change in wet weight was measured to be *ca.* 120% for SHE3350–AHE1500 and 155% for both SHE3350–AHE6000 and SHE3350–AHE6000 + AHE600, with no significant differences between these two formulations (Fig. 6). Then, buffer absorption reached a plateau starting from two weeks of incubation; the final changes in wet weight measured at 27 days of incubation were around 270%, 517% and 430% for SHE3350–AHE1500, SHE3350–AHE6000 and SHE3350–AHE6000 + AHE600, respectively. Moreover, the loss in dry weight after 27 days of incubation was quantified to be 32.3 ± 4.5% for SHE3350–AHE1500 (significantly lower than both SHE3350–AHE6000 and SHE3350–AHE6000 + AHE600,

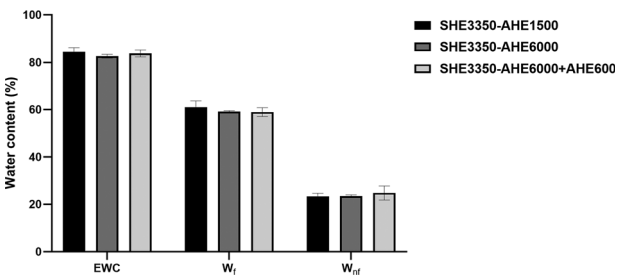

Fig. 4 Water content (%) of the developed Schiff-base hydrogels. Equilibrium water content (EWC), freezable water (W_f) content, and non-freezable water (W_{nf}) percentages estimated for SHE3350–AHE1500 (black bars), SHE3350–AHE6000 (grey bars) and SHE3350–AHE6000 + AHE600 (light grey bars).

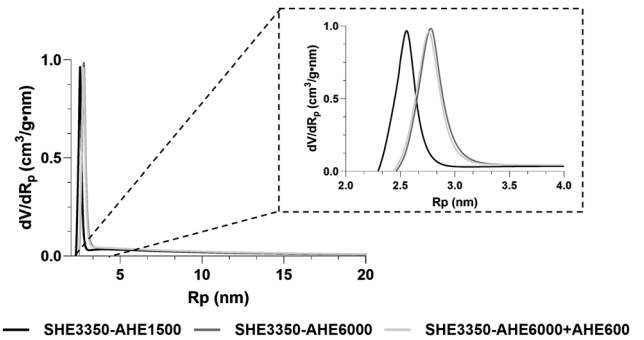

Fig. 5 Pore radii R_p (nm) distribution for SHE3350–AHE1500 (black line), SHE3350–AHE6000 (grey line) and SHE3350–AHE6000 + AHE600 (light grey line). The dash-dotted box highlights the magnification in the 2–4 nm range. The *Y* axis reports the pore volume distribution dV/dR_p ($cm^3\ g^{-1}\ nm^{-1}$).

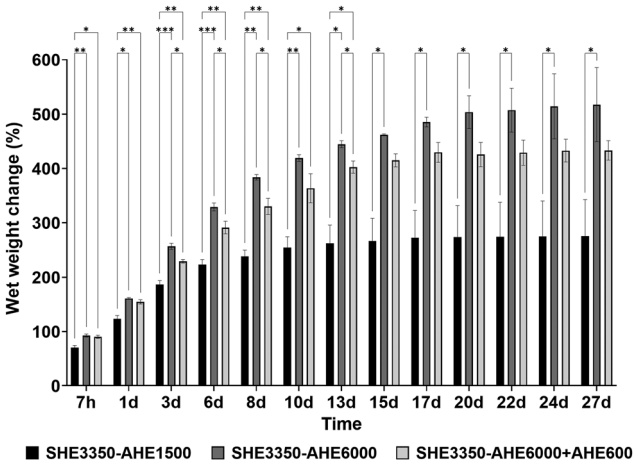

Fig. 6 Hydrogel wet weight change (%) as a function of time for SHE3350–AHE1500 (black bars), SHE3350–AHE6000 (grey bars) and SHE3350–AHE6000 + AHE600 (light grey bars) in contact with phosphate-buffered saline (pH 7.4, 37 °C). (*$p < 0.05$, **$p < 0.01$, ***$p < 0.001$).

$p < 0.05$), 42.7 ± 2.4% for SHE3350–AHE6000 and 46.9 ± 3.4% for SHE3350–AHE6000 + AHE600 (with no significant differences between the latter two formulations).

Since fluid absorption correlates with changes in wet weight of the hydrogel and consequently with changes in its volume and macroscopic dimension, the MRI technique was employed as a non-invasive and non-destructive tool to conduct a systematic study on the dimensional changes of the hydrogel over time.[38,39] To this purpose, a series of MRI analyses were performed at predefined time steps, and T_1- and T_2-weighted images were obtained. Sample dimensions along the longitudinal axis during swelling were quantified from T_1 and T_2-weighted MRI images (Fig. S6 and Fig. 7), with T_2-weighted images providing clear delineation of hydrogel boundaries. Fig. 8 reports the trends in dimensional change as a function of time evaluated from T_2-weighted images of SHE3350–AHE1500, SHE3350–AHE6000 and SHE3350–AHE6000 + AHE600 in contact with phosphate-buffered saline for up to 10 days of incubation. Monitoring fluid absorption after 1 day of incubation, an increase of around 15%, 33% and 27% in sample thickness was measured from T_2-weighted images for SHE3350–AHE1500, SHE3350–AHE6000, and SHE3350–AHE6000 + AHE600, respectively. After 10 days of incubation, the thickness of the hydrogels almost doubled, with dimension changes of around 52%, 71% and 65% measured from T_2-weighted images for SHE3350–AHE1500, SHE3350–AHE6000, and SHE3350–AHE6000 + AHE600, respectively. Consistently, the trends were completely in agreement with the change in wet weight data calculated through the gravimetric analysis of hydrogels incubated under the same experimental conditions. Indeed, the superior fluid absorption shown by SHE3350–AHE6000 was accompanied by enhanced dimensional changes, while the lowest dimension change was measured from the MRI images recorded for SHE3350–AHE1500, thus confirming that hydrogels with higher crosslinking density exhibited a

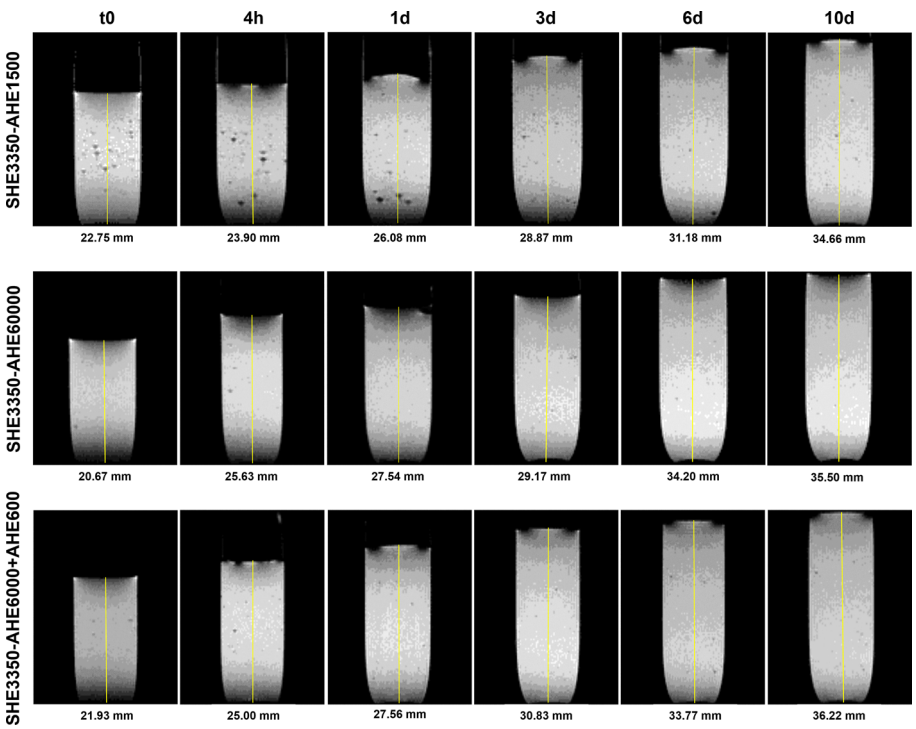

Fig. 7 T_2-weighted MRI images of SHE3350–AHE1500, SHE3350–AHE6000 and SHE3350–AHE6000 + AHE600 incubated in contact with phosphate-buffered saline (pH 7.4, 37 °C) for different time intervals (t_0, 4 h, 1, 3, 6 and 10 d). Yellow straight lines identify the performed measurements of sample size along the longitudinal axis.

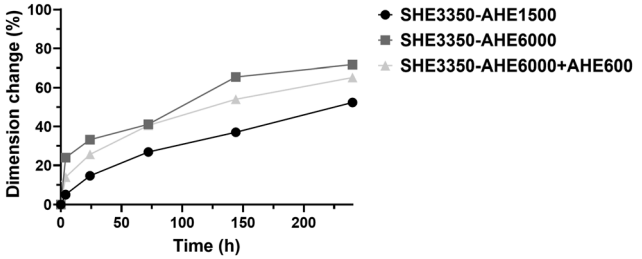

Fig. 8 Trend of dimension change (%) as a function of time measured from T_2-weighted MRI images of SHE3350–AHE1500, SHE3350–AHE6000 and SHE3350–AHE6000 + AHE600.

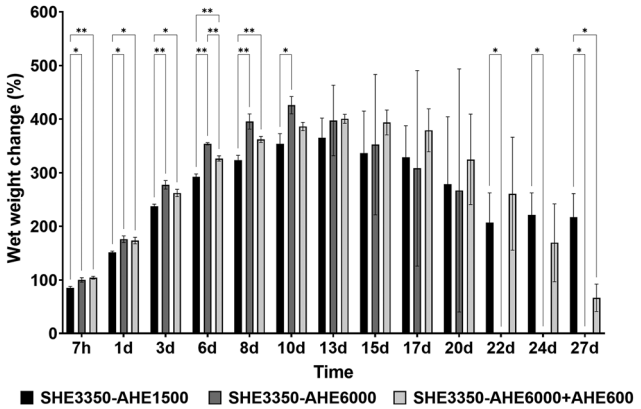

Fig. 9 Hydrogel wet weight change (%) as a function of time for SHE3350–AHE1500 (black bars), SHE3350–AHE6000 (grey bars) and SHE3350–AHE6000 + AHE600 (light grey bars) in contact with an acidic phosphate buffer (pH 5, 37 °C). (*$p < 0.05$, **$p < 0.01$, ***$p < 0.001$).

lower ability to absorb fluids and, consequently, lower changes in wet weight and volume over time.

Overall, although the three Schiff-base hydrogels displayed similar stability over time (dry weight loss in the range 32–47% after 27 days of incubation in contact with PBS), statistically significant differences in their abilities to absorb the buffer could be highlighted, due to the observed differences in the structural properties of the hydrogels. Indeed, the observed diversified behavior of the hydrogels in contact with a physiological-like environment was in accordance with the measured network parameters, thus providing additional evidence of the tunability of hydrogel mesh and, accordingly, its physical properties.

3.2.5. Schiff-base crosslinked hydrogels behaviour in contact with an acidic environment. Due to the intrinsic pH-responsiveness of the Schiff-base crosslinking, the evaluation of hydrogel behavior at pH 5 confirmed the sensitivity of the imine bond to acidic conditions, which trigger its progressive hydrolysis. The results confirmed that these Schiff-base hydrogels followed a bulk erosion model, where the penetration of the aqueous medium occurs faster than bond cleavage, leading to a uniform loss of crosslinking density throughout the matrix. Notably, a diversified dissolution kinetics was observed, strictly correlating with the specific hydrogel formulation and its mesh size. Overall, all three formulations exhibited a superior buffer absorption compared to the physiological-like conditions, although they were characterized by lower stability over time. At the early stage of incubation, SHE3350–AHE6000 and SHE3350–AHE6000 + AHE600 showed a wet weight gain of approximately 102%, significantly higher than the 85% recorded for SHE3350–AHE1500, characterized by the smallest mesh size ($p < 0.05$ and $p < 0.01$, respectively) (Fig. 9). The formulations reached maximum buffer absorption at approximately 13 days, with changes in wet weight of 360% for SHE3350–AHE1500 and up to 426% for SHE3350–AHE6000 and SHE3350–AHE6000 + AHE600. Beyond this peak, the progressive hydrolysis of the Schiff-base linkages led to a reversal in the weight trend, resulting in the gradual dissolution of the hydrogel network.

The long-term stability provided evidence of the remarkable acidic pH-sensitivity, which became more pronounced as the mesh size of the hydrogel increased. Consequently, SHE3350–AHE6000, characterized by the largest mesh size, achieved complete dissolution within 22 days (100% dry weight loss). In contrast, although the two formulations exhibited marked instability, SHE3350–AHE1500 and SHE3350–AHE6000 + AHE600 retained partial integrity up to 27 days, with dry weight losses of approximately 70% and 82%, respectively.

3.3. *In vitro* evaluation of release kinetics and diffusivity of probe molecules throughout the hydrogels

To further correlate the structural features of the hydrogel with the modulation of its physical properties, the diffusivity of probe molecules through the hydrogel network was studied to derive information on its structure.[26,40,41] In this scenario, the three Schiff-base hydrogels were investigated for their ability to release probe molecules of fluorescein isothiocyanate-dextran with increasing molecular weight. Release experiments were performed at pH 7.4 to evaluate the network in its highest stability state. While the pH-responsiveness of these systems was previously established,[24] testing at physiological pH allowed the investigation of mass transport governed by the network mesh size and its dynamic imine chemistry, minimizing the overlapping contribution of acid-induced matrix dissolution. Release kinetics and mechanisms were analyzed by applying the Korsmeyer–Peppas model. Furthermore, the diffusion mechanism of the molecules through the hydrogels was described through both theoretical and experimental approaches.

3.3.1. Study of release kinetics and mechanism of fluorescein isothiocyanate-dextran molecules. The release kinetics and mechanism of different fluorescein isothiocyanate-dextran molecules with molecular weight $\bar{M}_w$ of 4 kDa (FD4), 10 kDa (FD10) and 70 kDa (FD70) were investigated in physiological-like conditions (pH 7.4, 37 °C). The trends of FD4, FD10 and FD70 release from SHE3350–AHE1500, SHE3350–AHE6000 and SHE3350–AHE6000 + AHE600 were defined based on calibration curves built using standard solutions of FD at predefined concentrations (ranging between 0.025 mg mL^{-1} and 1 mg mL^{-1}). Concerning SHE3350–AHE1500, all the model molecules were released with a controlled and sustained

kinetics for up to 17 days of incubation (Fig. 10A). At the early stage of incubation, FD4 showed superior release compared to both FD10 and FD70, and the released FD4 at 24 hours of incubation was quantified to be 0.35 ± 0.015 mg mL^{-1}, significantly higher compared to FD10 (*i.e.*, 0.30 ± 0.005 mg mL^{-1}, $p < 0.01$) and FD70 (*i.e.*, 0.18 ± 0.04 mg mL^{-1}, $p < 0.01$). Starting from 6 days of incubation, the trends of FD4 and FD10 release became almost overlapped, and a maximum release of 0.87 ± 0.023 mg mL^{-1} and 0.83 ± 0.006 mg mL^{-1} was quantified for FD4 and FD10, respectively, after 17 days of incubation. Conversely, the amount of released FD70 was significantly lower than both FD4 (*i.e.*, at 6 days, 0.52 ± 0.08 mg mL^{-1} *vs.* 0.66 ± 0.02 mg mL^{-1}, $p < 0.01$) and FD10 (*i.e.*, at 3 days, 0.36 ± 0.06 mg mL^{-1} *vs.* 0.50 ± 0.005 mg mL^{-1}, $p < 0.01$).

Similar trends in model molecule release were observed from SHE3350–AHE6000 and SHE3350–AHE6000 + AHE600 (Fig. 10B and C, respectively). Indeed, for both the formulations, the FD4 and FD10 release profiles were comparable, with no significant differences. After 6 days of incubation, the FD4 and FD10 release reached a plateau, and the total amount of released molecules was achieved at 17 days of incubation. Overall, molecule release from SHE3350–AHE6000 formulation was characterized by higher release kinetics compared to those described for SHE3350–AHE1500. Indeed, at 24 hours of incubation the amount of released FD4, FD10 and FD70 was higher (*i.e.*, 0.49 ± 0.17 mg mL^{-1} *vs.* 0.35 ± 0.015 mg mL^{-1}, 0.54 ± 0.08 mg mL^{-1} *vs.* 0.30 ± 0.005 mg mL^{-1} and 0.27 ± 0.05 mg mL^{-1} *vs.* 0.18 ± 0.04, respectively). In this case, the recorded profiles of molecule release turned out to be clearly affected by the structural properties of the hydrogel, as the average mesh size of SHE3350–AHE6000 from the rheological data was significantly larger than that of SHE3350–AHE1500 (*i.e.*, *ca.* 50 nm *vs.* 18 nm). Furthermore, at the early stage of incubation, the amount of FD70 released from both SHE3350–AHE6000 and SHE3350–AHE6000 + AHE600 turned out to be significantly lower than that of FD4 and FD10 (*e.g.*, for SHE3350–AHE6000 at 24 hours, 0.27 ± 0.05 mg mL^{-1} *vs.* 0.49 ± 0.17 mg mL^{-1}, $p < 0.05$, and 0.54 ± 0.08 mg mL^{-1}, $p = 0.001$). Interestingly, for SHE3350–AHE6000 + AHE600, the amount of encapsulated FD70 was not completely released after 17 days of incubation. This result is in accordance with the reasonable assumption that the molecule release was obstructed by the irregular mesh of the hydrogel, formed by both high and low molecular weight AHE6000 and AHE600 PEUs. Hence, although the average mesh size (*ca.* 32 nm) was larger than the hydrodynamic diameter of FD70 (12 nm), and the hydrogel experienced swelling over time, the maximum FD70 release was quantified to be 0.74 ± 0.005 mg mL^{-1}. By applying the Korsmeyer–Peppas model, the release exponent n and the release constant k were calculated, as summarized in Table 4. The release exponent n for FD4 and FD10 from SHE3350–AHE1500 resulted to be 0.48 ± 0.005 and 0.49 ± 0.01, respectively, thus indicating a mechanism of molecule release prevalently governed by diffusion, with no significant differences between the two FD molecules. Conversely, the release exponent n and release constant k for FD70 were 0.57 ± 0.01 and 0.029 ± 0.003 h^{-n}, respectively, suggesting an anomalous molecule transport. These results suggest that the profile of molecule release and mechanism were probably affected not only by SHE3350–AHE1500 swelling, but also by the high molecular weight of FD70.[42] Regarding SHE3350–AHE6000 + AHE600, the release constant k for FD4 and FD10 was slightly higher than the values reported for SHE3350–AHE1500 (*i.e.*, 0.093 ± 0.02 h^{-n} *vs.* 0.07 ± 0.004 h^{-n} for FD4, 0.07 ± 0.004 h^{-n} *vs.* 0.068 ± 0.006 h^{-n} for FD10). These

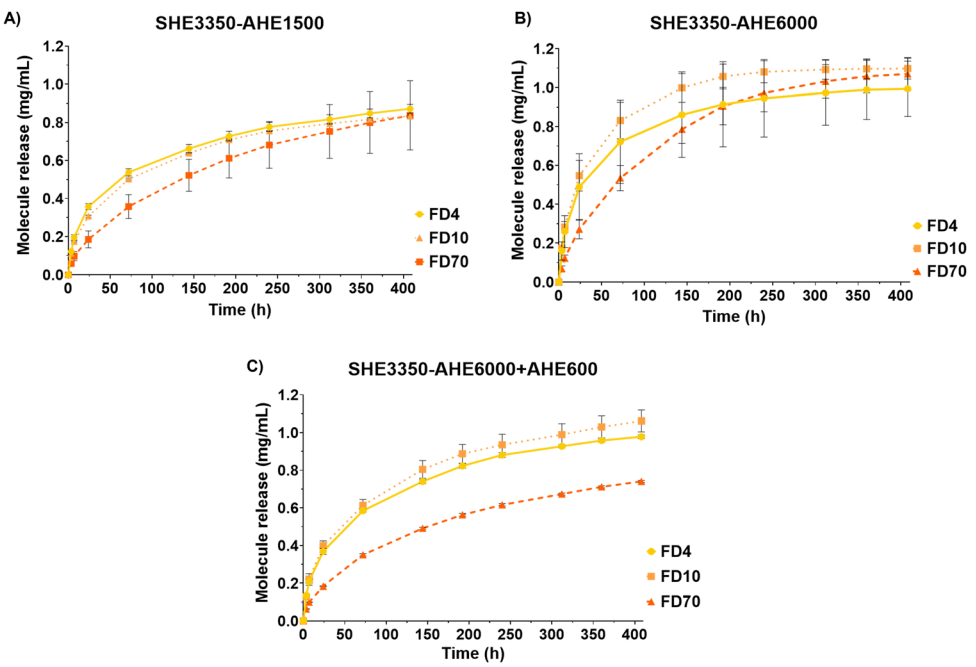

Fig. 10 FD4, FD10 and FD70 release profiles from (A) SHE3350–AHE1500, (B) SHE3350–AHE6000, and (C) SHE3350–AHE6000 + AHE600.

Table 4 Korsmeyer–Peppas model coefficients. Release constant k (h^{-n}) and release exponent n for FD4, FD10 and FD70 release from SHE3350–AHE1500, SHE3350–AHE6000, SHE3350–AHE6000 + AHE600

Sample	Model molecule	Korsmeyer–Peppas model	
		k (h^{-n})	n
SHE3350–AHE1500	FD4	0.07 ± 0.004	0.48 ± 0.005
	FD10	0.068 ± 0.006	0.49 ± 0.01
	FD70	0.029 ± 0.003	0.57 ± 0.01
SHE3350–AHE6000	FD4	0.08 ± 0.02	0.55 ± 0.07
	FD10	0.085 ± 0.005	0.58 ± 0.05
	FD70	0.031 ± 0.006	0.66 ± 0.02
SHE3350–AHE6000 + AHE600	FD4	0.093 ± 0.02	0.48 ± 0.02
	FD10	0.07 ± 0.004	0.5 ± 0.006
	FD70	0.033 ± 0.0008	0.54 ± 0.003

Table 5 Diffusion coefficients of fluorescein isothiocyanate-dextrans FD4, FD10 and FD70 through SHE3350–AHE1500, SHE3350–AHE6000 and SHE3350–AHE6000 + AHE600

Sample	D_0 ($\mu m^2 s^{-1}$)	D_p^* ($\mu m^2 s^{-1}$)	D_p ($\mu m^2 s^{-1}$)
		FD4	
SHE3350–AHE1500		199	3.57
SHE3350–AHE6000	234	210	—#
SHE3350–AHE6000 + AHE600		206	4
		FD10	
SHE3350–AHE1500		114	3.14
SHE3350–AHE6000	142	125	—#
SHE3350–AHE6000 + AHE600		122	4.7
		FD70	
SHE3350–AHE1500		33.6	—#
SHE3350–AHE6000	54	44.5	—#
SHE3350–AHE6000 + AHE600		41	—#

Theoretical diffusion coefficients in aqueous medium D_0 ($\mu m^2 s^{-1}$) calculated from eqn (10), expected diffusion coefficients through the hydrogel network D_p^* ($\mu m^2 s^{-1}$) calculated from the average mesh size using eqn (11), and experimental diffusion coefficients through the hydrogel network D_p ($\mu m^2 s^{-1}$) calculated from the release data using eqn (12). # stands for not applicable calculation (eqn (12) can be applied exclusively to diffusive release data).

discrepancies could be directly ascribed to differences in the structural parameters of the hydrogels, being the average mesh size of SHE3350–AHE1500 and SHE3350–AHE6000 + AHE600 around 18 nm and 32 nm, respectively, as calculated from rheological results. Moreover, the release exponent n turned out to be 0.48 ± 0.02 and 0.5 ± 0.006 for FD4 and FD10, respectively. Hence, although SHE3350–AHE6000 + AHE600 gel was characterized by an intermediate crosslinking density and, accordingly, swelling ability, it exhibited a mechanism of molecule release prevalently diffusion-driven, similar to SHE3350–AHE1500. Conversely, the mechanism of FD70 release from SHE3350–AHE6000 + AHE600 hydrogel was characterized by a release constant k of 0.033 ± 0.0008 h^{-n} and a mechanism of non-Fickian diffusion (*i.e.*, n of 0.54 ± 0.003), due to the high hydrogel absorption and the molecular weight of FD70 as concurrent factors.[42] Lastly, the release constant k values for each FD from SHE3350–AHE6000 were higher than those quantified for SHE3350–AHE1500 (*i.e.*, 0.08 ± 0.02 h^{-n} *vs.* 0.07 ± 0.004 h^{-n} for FD4, 0.085 ± 0.005 h^{-n} *vs.* 0.068 ± 0.006 h^{-n} for FD10, and 0.031 ± 0.006 h^{-n} *vs.* 0.029 ± 0.003 h^{-n} for FD70). Furthermore, due to its lower crosslinking density and higher capability for fluid absorption, the release mechanism of FD4, FD10 and FD70 was anomalous (*i.e.*, with an n value exceeding 0.5), even at the early stage of incubation.

3.3.2. Study of diffusion phenomena of fluorescein isothiocyanate-dextran molecules. The diffusivity of fluorescein isothiocyanate-dextran molecules through SHE3350–AHE1500, SHE3350–AHE6000 and SHE3350–AHE6000 + AHE600 was also thoroughly investigated. Firstly, to estimate the mobility of the probe molecules with different hydrodynamic radii R (1.4 nm, 2.3 nm and 6 nm for FD4, FD10 and FD70, respectively) through the hydrogel network, the diffusion coefficients were theoretically determined. Specifically, by applying the Lustig–Peppas model, diffusivity was related to the structure of each hydrogel network.[32] In detail, molecule diffusivities were measured based on the average mesh size of SHE3350–AHE1500, SHE3350–AHE6000 and SHE3350–AHE6000 + AHE600 calculated from rheological characterization and reported in Table 5. The expected diffusion coefficient D_p^* for FD4, FD10 and FD70 through the hydrogels turned out to be lower than the theoretical diffusion coefficient D_0, defined as the diffusion coefficients of the molecules in pure water and calculated according to the Stokes–Einstein equation. Indeed D_p^* values for FD4, FD10 and FD70 were affected by the presence of the polymeric network, which could restrict molecule diffusivity through the hydrogels. Moreover, as the molecular weight of the probe molecule increased, the diffusion coefficient decreased accordingly, and the diffusivity trends were in accordance with the release profiles of the model molecules described above. Indeed, irrespective of the formulation, the smaller FD4 and FD10 exhibited higher expected diffusion coefficients and release kinetics compared to the larger FD70, whose release profile was characterized by a lower release rate from each tested formulation (*e.g.*, for SHE3350–AHE1500, D_p^* of 199 $\mu m^2 s^{-1}$, 114 $\mu m^2 s^{-1}$ and 33.6 $\mu m^2 s^{-1}$ for FD4, FD10 and FD70, respectively). Furthermore, by comparing the diffusivity of the same molecule from each hydrogel network, the ratio of expected diffusivity to theoretical diffusivity, D_p^*/D_0, showed the following trend: SHE3350–AHE6000 > SHE3350–AHE6000 + AHE600 > SHE3350–AHE1500 (*e.g.*, for FD10 D_p^*/D_0 of 0.88, 0.85 and 0.80 for SHE3350–AHE6000, SHE3350–AHE6000 + AHE600 and SHE3350–AHE1500, respectively). Hence, it was hypothesized that the higher crosslinking density and lower mesh size of SHE3350–AHE1500 mostly hindered molecular transport. Nevertheless, although reasonable relationships were identified between the expected diffusion coefficients D_p^* of the probe molecules and the structural properties of the hydrogels derived from their rheological properties, the D_p^*/D_0 ratio showed approximately unitary values for all model molecules and formulations. This result suggested that the molecules could freely diffuse through the hydrogel network, as the average mesh size exceeded the hydrodynamic diameter of the selected model molecules

($\xi > 2R$). Conversely, by fitting the experimentally derived diffusive release data with an analytical solution of the Fick's second law of diffusion, the diffusion coefficients were also empirically derived. The experimental diffusion coefficient D_p of FD4 and FD10 through the hydrogels was found to be much lower than the expected values D_p^*, as reported in Table 5. Indeed, as the release mechanism was described as prevalently diffusive, D_p was estimated to be 3.57 $\mu m^2 s^{-1}$ and 4 $\mu m^2 s^{-1}$ for FD4, and 3.14 $\mu m^2 s^{-1}$ and 4.7 $\mu m^2 s^{-1}$ for FD10, through SHE3350–AHE1500 and SHE3350–AHE6000 + AHE600, respectively. In this case, the ratio of experimental diffusivity to theoretical diffusivity, D_p/D_0, was much lower than the unitary value ($D_p/D_0 \ll 1$), thus suggesting that the transport of the molecules through the hydrogel network was strongly affected by the presence of the polymer chains.[43] The discrepancy between the theoretical and experimental approaches in determining the diffusivity of the model molecules could be attributed to the inherent divergence of the Schiff-base network from the idealized conditions assumed by the Lustig–Peppas model. While the determination of the expected diffusivity coefficient $\left(D_p^*\right)$ relied on an average mesh size, in turn predicted from the rubber elasticity theory and the rheological properties of the hydrogels, this approximation overlooked the complex arrangement and entanglements of the polymeric chains. In particular, the specific polydispersity of the PEU precursors resulted in a network architecture characterized by a broad distribution of mesh sizes, arising from the intrinsically heterogeneous length of the polymer chains between crosslinking points. This network architecture created local diffusion barriers that were not considered in the theoretical framework. Furthermore, the dynamic nature of the Schiff-base linkages introduced a dynamic reorganization of the hydrogel network; the continuous exchange of imine bonds could facilitate transient chain mobility and the potential entrapment of solutes. Such phenomena further reduced the experimental diffusion coefficients compared to the static theoretical predictions, shifting the transport of molecules toward a network-hindered regime.

3.4. Hydrogel morphological characterization

The morphological characterization of freeze-dried Schiff-base hydrogels was performed through Scanning Electron Microscopy (SEM) and provided information about their structure and properties. Indeed, by analyzing the microstructure and porosity of the hydrogel, the arrangement and density of the polymer network can be determined and correlated with their mechanical properties and functional performance, including fluid transport, diffusion and swelling.[44] As shown in Fig. 11, all the hydrogels were characterized by high porosity, with interconnected pores and honeycomb-like structure. SHE3350–AHE1500, SHE3350–AHE6000 and SHE3350–AHE6000 + AHE600 (Fig. 11A–C, respectively) displayed irregular size of the pores proportional to the size of the ice crystals which formed during the freezing phase, with wider pores in SHE3350–AHE6000 compared to the other formulations. Furthermore, considering that the same methodology was applied to freeze all the gel samples at −20 °C, differences in morphology can be related to the diversified compositions and structure of the gels. Indeed, by comparing the SEM images, a relationship between the crosslinking density of the hydrogel and the porosity of the freeze-dried sample was identified. As the crosslinking density was lower, the porosity of the freeze-dried samples was higher (*i.e.*, porosity of SHE3350–AHE6000 > SHE3350–AHE6000 + AHE600 > SHE3350–AHE1500).

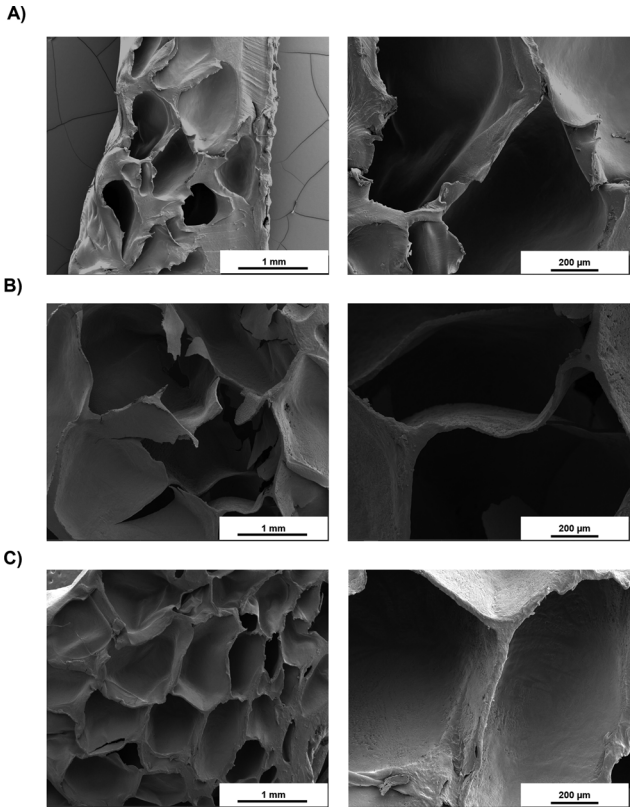

Fig. 11 Scanning Electron Microscopy (SEM) images of freeze-dried hydrogels: (A) SHE3350–AHE1500, (B) SHE3350–AHE6000, and (C) SHE3350–AHE6000 + AHE600 at different magnifications (30× on the left, 100× on the right).

Conclusions

In this work, the mesh size of Schiff-base hydrogels was successfully modulated by customized aldehyde-terminated poly(ether urethane)s. Accordingly, the effective tuning of the physico-chemical and rheological properties, as well as the solute transport throughout the hydrogels, was demonstrated by combining different methodologies for the hydrogel characterization. Rheological characterization evidenced that all the developed formulations displayed high resistance to applied deformation although their mechanical response was diversified. By correlating their elastic response to the structural properties of the hydrogels (crosslinking density and mesh size), the formulation of Schiff-base hydrogels with small, medium and large mesh sizes was demonstrated. Furthermore, as evidenced by stability tests of hydrogels in contact with an

aqueous environment, the tunability of the hydrogel mesh size resulted in diversified fluid absorption, as an increased mesh size led to increased swelling ability. Lastly, the diffusivity of different probe molecules (fluorescein isothiocyanate-dextran with molecular weight of 4, 10 or 70 kDa) within the hydrogel was theoretically modeled and experimentally determined. Discrepancies between theoretical and experimental values were observed, highlighting the key role of the arrangement of the polymer chains, entanglements, and the overall heterogeneity of the hydrogel network in determining the effective molecule diffusivity through the hydrogels. In conclusion, the proposed modifications in hydrogel composition resulted in easily tunable internal structure, properties and performance of the hydrogels. These characteristics make the developed formulations highly versatile and well-suited for satisfying specific requirements as advanced biomaterials for tissue engineering and regenerative medicine, with potential applications including diffusion-controlled or stimuli-responsive drug delivery, and the engineering of specific tissues such as cartilage, skin, or vascularized constructs.

Author contributions

The manuscript was written through contributions of all authors. All authors have given approval to the final version of the manuscript. Conceptualization, R. P. and M. B.; methodology, R. P., M. B., C. C., A. F., I. C.; validation, R. P., M. B.; formal analysis, R. P., M. B., C. C., A. F., I. C.; resources, G. C., L. M.; data curation, R. P., M. B.; writing-original draft preparation, R. P.; writing-review and editing, M. B., C. C., A. F., L. M., I. C., V. C., G. C.; visualization, R. P.; supervision, V. C., G. C.; funding acquisition G. C.

Conflicts of interest

The authors declare no conflicts of interest.

Data availability

All relevant data are within the manuscript and supplementary information (SI). Supplementary information: methods and results of the chemical characterization of poly(ether urethane)s (PEUs) (ATR-FTIR spectroscopy, size exclusion chromatography, ^{1}H NMR spectroscopy); schematic illustration of the PEU precursors and the mechanism of formation of Schiff-base hydrogels; methods and results of the thermal characterization of hydrogels (estimation of pore size distribution and thermal transition data); T_1-weighted MRI images of hydrogels. See DOI: https://doi.org/10.1039/d6ma00816j.

The data are available from the corresponding author on reasonable request.

Acknowledgements

The research leading to these results has received funding from the European Union-NextGenerationEU through the Italian Ministry of University and Research under PNRR-M4C2-I1.3 Project PE00000019 ''HEAL ITALIA'' to Gianluca Ciardelli CUP E93C22001860006 of Università di Modena e Reggio Emilia. The view and opinions expressed are those of the authors only and do not necessarily reflect those of the European Union or European Commission. Neither the European Union nor the European Commission can be held responsible for them. The authors acknowledge the Multi Modal Molecular Imaging (MMMI) Italian Node of the Eurobioimaging Research Infrastructure for supporting the 7 T ultra-high-field magnetic resonance imaging facility of the ''G. Monasterio'' Foundation. The authors also thank Elena Cunietti for assistance in data collection.

References

1 W. A. Laftah, S. Hashim and A. N. Ibrahim, *Polym. Plast. Technol. Eng.*, 2011, **50**, 1475–1486.
2 A. S. Hoffman, *Adv. Drug Delivery Rev.*, 2012, **64**, 18–23.
3 N. Sood, A. Bhardwaj, S. Mehta and A. Mehta, *Drug Delivery*, 2016, **23**, 748–770.
4 H. Khonakdar, M. Ehsani, G. Naderi, F. Shokrolahi and H. A. Khonakdar, *J. Polym. Environ.*, 2025, **33**, 3512–3554.
5 E. Yun and C. Cha, *J. Mater. Chem. B*, 2026, **14**, 8398–8407.
6 R. Parhi, *Adv. Pharm. Bull.*, 2017, **7**, 515–530.
7 V. S. Raghuwanshi and G. Garnier, *Adv. Colloid Interface Sci.*, 2019, **274**, 102044.
8 P. Lu, D. Ruan, M. Huang, M. Tian, K. Zhu, Z. Gan and Z. Xiao, *Signal Transduct. Target. Ther.*, 2024, **9**, 166.
9 N. Kamaly, B. Yameen, J. Wu and O. C. Farokhzad, *Chem. Rev.*, 2016, **116**, 2602–2663.
10 M. A. K. Tolentino, E. Y. Du, G. Silvani, E. Pandzic, K. A. Kilian and J. J. Gooding, *Adv. Healthcare Mater.*, 2025, **14**, 2500658.
11 F. Bisotti, F. Pizzetti, G. Storti and F. Rossi, *Drug Delivery Transl. Res.*, 2022, **12**, 1928–1942.
12 M. H. Kim, J. N. Lee, J. Lee, H. Lee and W. H. Park, *ACS Biomater. Sci. Eng.*, 2020, **6**, 3103–3113.
13 T. Bal, B. Kepsutlu and S. Kizilel, *J. Biomed. Mater. Res. - Part A*, 2014, **102**, 487–495.
14 J. Xia, Z. Y. Liu, Z. Y. Han, Y. Yuan, Y. Shao, X. Q. Feng and D. A. Weitz, *Acta Biomater.*, 2022, **141**, 178–189.
15 T. Wang, G. Qu, C. Wang, Y. Cheng, J. Shang, J. Zheng, Z. Feng, Q. Chen and N. He, *Langmuir*, 2019, **35**, 13999–14006.
16 M. Caldorera-Moore, K. Maass, R. Hegab, G. Fletcher and N. Peppas, *J. Drug Delivery Sci. Technol.*, 2015, **30**, 352–359.
17 M. S. Rehmann, K. M. Skeens, P. M. Kharkar, E. M. Ford, E. Maverakis, K. H. Lee and A. M. Kloxin, *Biomacromolecules*, 2017, **18**, 3131–3142.
18 X. Tong, S. Lee, L. Bararpour and F. Yang, *Macromol. Biosci.*, 2015, **15**, 1679–1686.
19 L. Bian, C. Hou, E. Tous, R. Rai, R. L. Mauck and J. A. Burdick, *Biomaterials*, 2013, **34**, 413–421.
20 M. Boffito, E. Gioffredi, V. Chiono, S. Calzone, E. Ranzato, S. Martinotti and G. Ciardelli, *Polym. Int.*, 2016, **65**, 756–769.

21 A. Torchio, M. Boffito, A. Gallina, M. Lavella, C. Cassino and G. Ciardelli, *J. Mater. Chem. B*, 2020, **8**, 7696–7712.
22 A. Torchio, C. Cassino, M. Lavella, A. Gallina, A. Stefani, M. Boffito and G. Ciardelli, *Mater. Sci. Eng., C*, 2021, **127**, 112194.
23 R. Laurano and M. Boffito, *Front. Bioeng. Biotechnol.*, 2020, **8**, 1–14.
24 R. Pappalardo, M. Boffito, C. Cassino, V. Caccamo, V. Chiono and G. Ciardelli, *ACS Omega*, 2024, **9**, 45774–45788.
25 Y. Tsuji, X. Li and M. Shibayama, *Gels*, 2018, **4**(2), DOI: 10.3390/gels4020050.
26 J. Karvinen, T. O. Ihalainen, M. T. Calejo, I. Jönkkäri and M. Kellomäki, *Mater. Sci. Eng., C*, 2019, **94**, 1056–1066.
27 W. Ali, B. Gebert, S. Altinpinar, T. Mayer-Gall, M. Ulbricht, J. S. Gutmann and K. Graf, *Polymers*, 2018, **10**, 1–21.
28 X. Yang, B. L. Dargaville and D. W. Hutmacher, *Polymers*, 2021, **16**(6), DOI: 10.3390/polym13060845.
29 R. Manikoth, I. Kanungo, N. N. Fathima and J. R. Rao, *Carbohydr. Polym.*, 2012, **88**, 628–637.
30 I. S. Raja and N. N. Fathima, *SpringerPlus*, 2014, **3**, 1–10.
31 R. Laurano, A. Torchio, G. Ciardelli and M. Boffito, *Gels*, 2023, **9**(9), DOI: 10.3390/gels9090731.
32 F. Brandl, F. Kastner, R. M. Gschwind, T. Blunk, J. Teßmar and A. Göpferich, *J. Controlled Release*, 2010, **142**, 221–228.
33 S. Koutsopoulos, L. D. Unsworth, Y. Nagai and S. Zhang, *Proc. Natl. Acad. Sci. U. S. A.*, 2009, **106**, 4623–4628.
34 J. Wang and V. M. Ugaz, *Electrophoresis*, 2006, **27**, 3349–3358.
35 C.-W. Chang, B. L. Dargaville, K. I. Momot and D. W. Hutmacher, *J. Mater. Chem. B*, 2024, **12**, 6328–6341.
36 Y. Xia, H. Cho, M. Deo, S. H. Risbud, M. H. Bartl and S. Sen, *Sci. Rep.*, 2020, **10**, 1–8.
37 A. C. Sparavigna, *SSRN Electronic Journal*, 2023, 1–16, DOI: 10.2139/ssrn.4349640.
38 A. Prior-Cabanillas, J. M. Barrales-Rienda, G. Frutos and I. Quijada-Garrido, *Polym. Int.*, 2007, **56**, 506–511.
39 S. Haas, B. Schmieg, P. Wendling, G. Guthausen and J. Hubbuch, *Polymers*, 2022, **14**(22), DOI: 10.3390/polym14225023.
40 M. Wallace, D. J. Adams and J. A. Iggo, *Soft Matter*, 2013, **9**, 5483–5491.
41 R. Zhang, Y. Tao, W. Xu, S. Xiao, S. Du, Y. Zhou and A. Hasan, *Int. J. Biol. Macromol.*, 2018, **120**, 2399–2409.
42 C. S. Brazel and N. A. Peppas, *Polymer*, 1999, **40**, 3383–3398.
43 S. Limem and P. Calvert, *J. Mater. Chem. B*, 2015, **3**, 4569–4576.
44 F. D. Martinez-Garcia, T. Fischer, A. Hayn, C. T. Mierke, J. K. Burgess and M. C. Harmsen, *Gels*, 2022, **8**, 1–20.

